ACS Catalysis

pubs.acs.org/acscatalysis

Research Article

Detection of Spontaneous FeOOH Formation at the Hematite/Ni(Fe)OOH Interface During Photoelectrochemical Water Splitting by Operando X-ray Absorption Spectroscopy

Ahmed S. M. Ismail,* Ivan Garcia-Torregrosa, Jeroen C. Vollenbroek, Laura Folkertsma, Johan G. Bomer, Ties Haarman, Mahnaz Ghiasi, Meike Schellhorn, Maarten Nachtegaal, Mathieu Odijk, Albert van den Berg, Bert M. Weckhuysen, and Frank M. F. de Groot*

Cite This: *ACS Catal.* 2021, 11, 12324–12335

Read Online

ACCESS | Metrics & More | Article Recommendations | Supporting Information

ABSTRACT: The role that the α-Fe_2O_3/NiFeOOH interface plays in dictating the oxygen evolution reaction (OER) mechanism on hematite has been a source of intense debate for decades, but the chemical characteristics of this interface and its function are still ambiguous and subject to speculation. In this study, we employed operando X-ray absorption spectroscopy to investigate the interfacial dynamics at the α-Fe_2O_3/NiFeOOH interface. We uncovered the spontaneous formation of a FeOOH interfacial layer under (photo)electrochemical conditions. This FeOOH interfacial layer plays a role in the surface passivation of hematite and in accumulating the (photo)generated holes upon external potential application. This hole-accumulation process leads to the extraction of more (photo)generated holes from hematite before releasing them to NiFeOOH to carry out the water-splitting reaction, and it also explains the reason for the delay in the nickel oxidation process. Based on these observations, we propose a model where NiFeOOH acts mainly as an OER catalyst and a facilitator of holes extraction from hematite, while the interfacial FeOOH layer acts as a surface passivation and hole-accumulation overlayer.

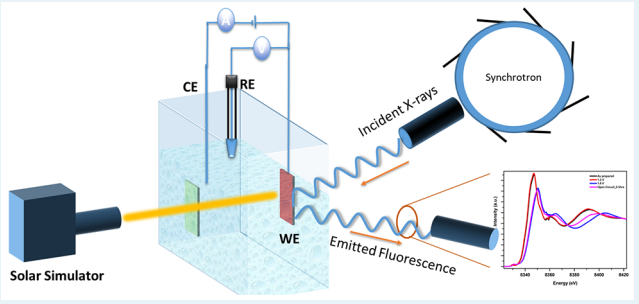

KEYWORDS: *water splitting, catalysts, operando X-ray spectroscopy, nickel iron oxyhydroxide, hematite, interface, iron oxyhydroxide*

INTRODUCTION

The oxygen evolution reaction (OER) in the water-splitting process is the main reason for the larger overpotential necessary to split water into oxygen and hydrogen. The OER involves four proton-coupled electron transfers and oxygen–oxygen bond formation, resulting in sluggish kinetics and the need for a catalyst to improve the reaction efficiency. Here, 4d and 5d transition metal oxides, such as RuO_2 and IrO_2, are well-known state-of-the-art OER catalysts rendering a relatively low overpotential and high stability in acidic media.[1−4] However, the scarcity and high cost of Ir and Ru metals are the main constraints for the development of industrially relevant applications for electrochemical hydrogen production.

Ni–Fe-based electrocatalysts have shown catalytic efficiencies surpassing those of the IrO_2 catalyst in alkaline media.[4−8] As a result, highly active and durable Ni–Fe-based electrocatalysts were prepared by cathodic and anodic electrodeposition and have shown remarkably low OER overpotentials.[9,10] Trotochaud et al. investigated the influence of iron concentration in $Ni(OH)_2$ thin films prepared by a solution-cast method, where $Ni_{0.9}Fe_{0.1}O_x$ compositions were found to be among the most active water oxidation catalysts in basic media with a Tafel slope of 30 mV dec^{-1} and OER activities an order of magnitude higher than IrO_x control films.[11] Interestingly, it was shown that the electronic conductivity of the films increased by a factor of 30 after the intentional addition of Fe impurities. Several later studies have focused on understanding the role of Fe addition on the OER performance enhancement in NiOOH catalysts. Some studies suggested that incorporating even a small concentration of Fe in NiOOH resulted in the substitution of the Ni sites in NiO_6 octahedra by Fe, where Fe species become the active sites for OER.[12,13] Other studies suggested that the role of Fe involves mainly accelerating the OER process by acting as a Lewis acid that promotes the oxidation of Ni^{2+} to Ni^{4+}.[14] In the center of this debate lies the main question about whether high valent metal species, such as Fe^{4+}, could form under OER conditions,

Received: June 8, 2021
Published: September 20, 2021

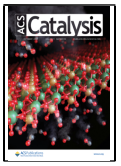

https://doi.org/10.1021/acscatal.1c02566
ACS Catal. 2021, 11, 12324–12335

where it could promote the formation of high valent Ni^{4+} or act directly as OER active sites. Nevertheless, the majority of reported literature agrees on the crucial role the Fe plays in reducing the OER overpotential in NiFeOOH. For a deeper insight into the evolution of the electronic structure of NiFeOOH during OER, the reader is referred to excellent reviews on this topic.[8,15,16]

Deposition of NiFeOOH OER catalysts on hematite semiconductors has been generally shown to lower the OER photocurrent onset potential of hematite.[17,18] However, the exact role that these catalysts (or overlayers) play in improving the OER performance of hematite is poorly understood, mainly due to the nontraditional structure of these electrocatalysts (i.e., unlike the well-defined structure of metal oxide semiconductors, electrocatalysts are often layered, porous, and hydrated), which makes the characterization of their structure and OER mechanism cumbersome. Moreover, the lack of available experimental tools that can directly investigate interfacial processes is an additional challenge to the semiconductor/catalyst characterization efforts. Several reports suggested that thin films made of NiFeOOH act as direct OER catalysts that play a major role in the process by extracting the photogenerated holes from α-Fe_2O_3 and utilizing them to drive OER.[19−21] Others reported that these overlayers mainly assist hematite in driving OER at lower onset potential by passivating surface defects and slowing the rate of surface recombination, hence reducing the electron-hole recombination probability, which leads to a higher concentration of holes available for OER at the semiconductor surface.[10,22−26] Additionally, A third group suggested that NiFeOOH could play both roles.[27] All of these reports highlight the importance of understanding the role of the semiconductor/catalyst interface in dictating the overall performance of the hematite OER performance, which is crucial for future realization of efficient water-splitting photoanodes.[17,28] Although several characterization studies have been reported on the semiconductor/catalyst interfaces, few of them were focused on the characterization of the combined α-Fe_2O_3/NiFeOOH system. Malara et al. conducted electrochemical studies on the system and concluded that the anodic wave formed in the cyclic voltammogram scan at a potential of ∼1.2 V_{RHE} is due to the possible formation of a new α-Fe_2O_3/NiFeOOH interface that is associated with the Ni redox waves and is considered an indirect evidence that this Ni redox process induced a new recombination process at the α-Fe_2O_3/NiFeOOH interface.[28] Another notable example is the work of Laskowski et al., who utilized a dual-electrode photo-electrochemistry method that could directly track the current generated on the catalytic overlayer during the photoelectrochemical OER.[29] They concluded that NiFeOOH can act as both an overlayer for holes collection and as a catalyst that drives OER by showing that NiFeOOH was oxidized by the photogenerated holes at a rate that is compatible with OER operating potentials. A previous work by the same group shed light on the importance of eliminating possible pinholes in mesoporous semiconductors through which the deposited NiFeOOH overlayers could become in direct contact with the back contact that effectively acts as a recombination center for the photogenerated holes.[30] In another study, George et al. conducted density functional theory + U calculations to understand the role of NiOOH catalyst in improving the OER performance of hematite. They reached a conclusion that the improved OER performance in NiOOH-α-Fe_2O_3 system stems from the Ni edge sites that are in close proximity to Fe in hematite.[31]

Operando X-ray absorption spectroscopy (XAS) is the main characterization tool utilized in this work to investigate the electronic structure dynamics in α-Fe_2O_3 and NiFeOOH during OER. This method has been used with great success in the last few years in characterizing water-splitting electrodes because of its element- specificity combined with its ability to track even the small changes in oxidation state and local structure around the absorbing atom under operational conditions.[32] Braun et al. conducted one of the first operando XAS studies on the oxygen K-edge in hematite photoanodes.[33,34] They identified two types of photogenerated hole transitions taking place under OER onset potential; an O 2p hole transition to the charge-transfer band and a Fe 3d transition into the upper Hubbard band. They concluded that both types of holes directly contribute to the photocurrent generated on hematite during OER. Another notable example is the work of Friebel et al. on F:SnO_2/NiFeOOH, where Fe^{3+} was reported to occupy octahedral sites with very short Fe−O bond distances surrounded by edge-sharing [NiO_6] octahedra, which in turn render these Fe sites near-optimal adsorption energies of OER intermediates. Therefore, it was concluded that Fe sites were active for the OER, and by their incorporation, Ni oxidizes to an "average" oxidation state of $Ni^{3.6}$ and that Ni sites play a less important role during OER.

In this work, we studied the role of NiFeOOH in promoting OER on hematite by conducting operando X-ray absorption spectroscopy on both F:SnO_2 (will be referred to as FTO)/NiFeOOH and α-Fe_2O_3/NiFeOOH electrodes during electrochemical/photoelectrochemical water oxidation at pH 13.6. The goal of this work is to disentangle the chemical and structural changes that take place on both NiFeOOH and α-Fe_2O_3, and their interface during OER and the effect of solar-simulated illumination in this process. We detected the spontaneous formation of FeOOH layer at the α-Fe_2O_3/NiFeOOH interface under (photo-)electrochemical OER conditions, which possibly plays a major role in dictating the charge carrier transfer across the interface. Based on the study results, we also speculate on the main general electronic and structural characteristics of a future efficient OER catalyst.

EXPERIMENTAL SECTION

For this study, two working electrodes were designed: SiN_x/FTO/(Ni,Fe)O_x and SiN_x/FTO/α-Fe_2O_3/NiFeOOH combined semiconductor/electrocatalyst systems. Briefly, 1.4 μm of free-hanging SiN_x membranes were prepared by deposition of a layer of low-stress SiN_x, followed by etching through a ⟨111⟩ silicon substrate using KOH. Two different electrode designs were made depending on the photoelectrochemical reactor employed in the operando XAS measurements. The first type contained both working electrode and counter electrode on the same silicon chip (Figure S1a). Extreme care has been taken to avoid short circuiting both electrodes during deposition and reaction (Supporting Information Section 1). The second type contained only the working electrode on the Si chip, while the Pt counter electrode was inserted in the separate inlet in the reactor (Figure S1b). An electron conductive fluorine-doped tin (FTO) oxide layer (150 nm) was then deposited on certain areas in the SiN_x membranes by ultrasonic spray pyrolysis from a water-based solution comprised of NH_4F and $SnCl_4$ salts. A 50 nm (Ni,Fe)O_x permeable thin-film catalyst was deposited on ∼150 nm FTO

https://doi.org/10.1021/acscatal.1c02566
ACS Catal. 2021, 11, 12324−12335

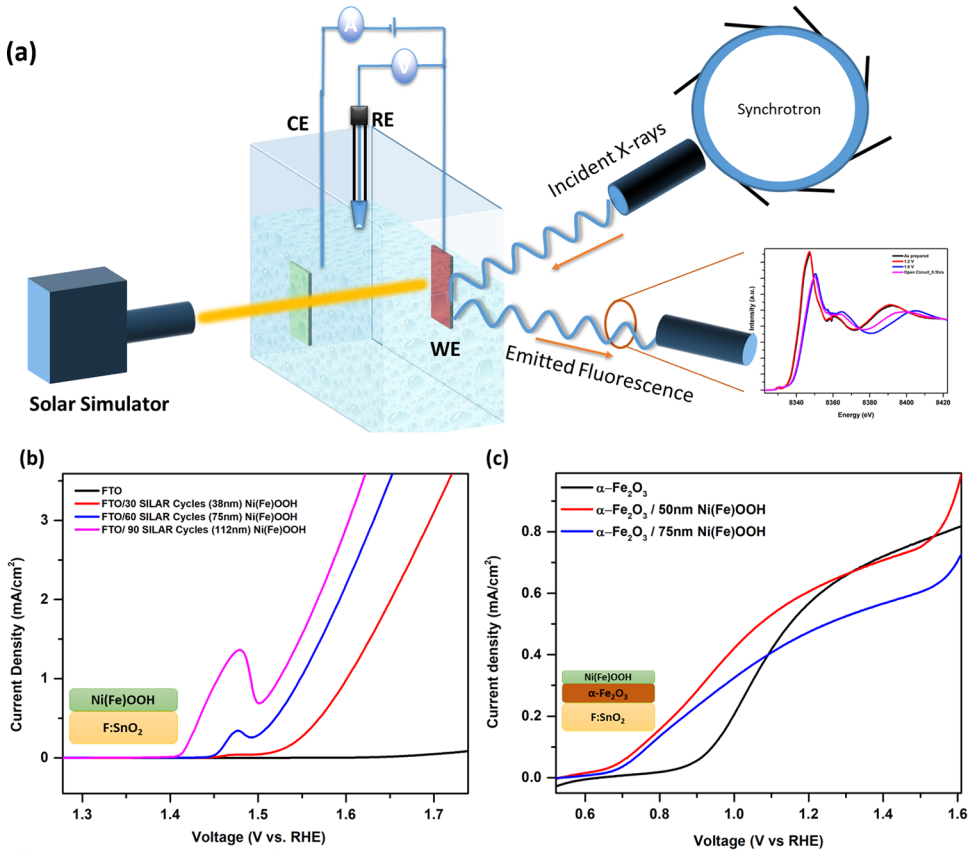

Figure 1. Operando X-ray absorption spectroscopy (XAS) setup and photoelectrochemical measurements of the FTO/$Ni_{0.8}Fe_{0.2}OOH$ catalyst and α-Fe_2O_3/$Ni_{0.8}Fe_{0.2}OOH$ photoanode. (a) Schematic representation of the operando XAS experiment during photoelectrochemical (PEC) water splitting. During the measurement, solar-simulated optical illumination was focused on the sample (brown color in the figure) from the front direction through a transparent quartz window (pale green). (b) Linear sweep voltammetry (LSV) of several FTO/$Ni_{0.8}Fe_{0.2}OOH$ catalysts prepared with different number of SILAR (successive ionic adsorption and reaction) cycles. (c) LSV of bare hematite (black), α-Fe_2O_3/50 nm $Ni_{0.8}Fe_{0.2}OOH$ film (red), and α-Fe_2O_3/75 nm $Ni_{0.8}Fe_{0.2}OOH$ film (blue). The inset in each panel shows schematics of the working electrodes. All of the LSV scans were recorded at 1 M NaOH at a scan rate of 10 $mV{\cdot}s^{-1}$. The potential in the measurements is reported vs the reversible hydrogen electrode. The samples in panel (c) were illuminated with ~100 $mW{\cdot}cm^{-2}$ of AM1.5G solar-simulated optical light.

using successive ionic layer adsorption and reaction (SILAR). To prepare the cation solution, a mixture of $FeCl_2$ (Sigma-Aldrich, 98% purity) and $NiCl_2$ $(H_2O)_6$ (Merck, 98% purity) with Fe/Ni ratio of 1:5 was dissolved in distilled water (18 MΩ cm^{-1}), while the anion solution was prepared by dissolving 0.1 M NaOH in distilled water (18 MΩ cm^{-1}). A typical deposition cycle consisted of a 10 s immersion in (1) cation solution, (2) distilled water (rinsing), (3) anion solution, and (4) distilled water. For the preparation of hematite thin films, Fe(III) acetylacetonate (acac) (Acros, >99% purity) was dissolved in ethanol (Interchem, 100% purity) under strong stirring for 12 h at a concentration of 50 mM. A custom-made ultrasonic spray pyrolysis chamber was used for the direct deposition of 100 nm hematite thin film at a deposition temperature of 420 °C and a flow rate of 3 mL min^{-1}. To compare the electrochemical properties of the samples in the reactor with the laboratory setup, the working electrode was deposited on mechanically and chemically cleaned-fluorine-doped tin oxide (FTO) coated borosilicate glass (Pilkington, TEC 15). The thickness and morphology of the prepared samples were then characterized with X-ray diffraction (XRD), scanning electron microscopy fitted with energy-dispersive X-ray spectroscopy (SEM-EDX) (Supporting Information Section 2).

For the operando Fe and Ni K-edge X-ray absorption experiment, two different photoelectrochemical cells were prepared. The first type is a commercially available flow cell (DRP-FLWCL, DropSens, Spain) that was modified to satisfy the requirements of the XAS experiment. The original flow inlet was sealed with a mica window (diameter 4 mm, thickness ~20 μm) and served as an entrance window for the optical beam originating from the solar simulator (Figure S3). A conical beam entrance and exit window was drilled in the base plate of the cell so that it allows the incident X-ray beam and the fluorescent signal to enter and exit the silicon nitride windows from the back side of the electrode at an angle of ~45°. A liquid flow inlet and outlet were drilled on the side of the cell to allow electrolyte flow during the photoelectrochemical measurements. The original flow inlet was redesigned to contain the Ag/AgCl reference electrode (3 M KCl, liquid junction, Metrohm, Switzerland). Prior to the measurements, the cell was filled with the electrolyte, and a constant flow of the electrolyte (2 mL min^{-1}) was maintained throughout the experiment. This was also useful to eliminate any oxygen bubbles formed during the water-splitting process. To test the reproducibility of the results and to confirm that there are no spectral artifacts resulting from possible interaction between the incident X-ray beam and the photoelectrochemical cell, a custom-made static electrolyte high-density polyethylene-based

https://doi.org/10.1021/acscatal.1c02566
ACS Catal. 2021, 11, 12324−12335

reactor was employed, where two orifices were drilled into the cap to serve as inlets for the coiled Pt wire counter electrode (Sigma-Aldrich) and the Ag/AgCl/3 M KCl reference electrode (Metrohm, Switzerland) (Figure S3). Two 8 mm diameter orifices were drilled on opposite sides of the bottle. In the first orifice, a 1.4 μm silicon nitride window that contained the working electrode (FTO/$Ni_{1-x}Fe_xOOH$) was fixed using epoxy resin. In the opposite orifice, a transparent 1 mm thick fused silica substrate was fixed with epoxy resin to allow for the optical light to illuminate the working electrode from the front side when needed (Supporting Information Section 3). The working electrode area in contact with the electrolyte is 8 mm in the static electrolyte reactor and 10 mm in the liquid flow reactor.

Prior to the XAS measurements, cyclic voltammetry scans were recorded to investigate the current response of the semiconductor, the co-catalyst, and the combined system using a three-electrode configuration. An external voltage was applied using a potentiostat (CompactStat, Ivium Technologies, The Netherlands) in the range from 0 to 1.8 V vs RHE with a scan rate of 50 mV s^{-1}. During the XAS measurements, chronoamperometry measurements were performed at 0.4, 0.8, 1.2, 1.6, and 1.8 V vs RHE (Figure S4). The alkaline electrolyte used was a 1 M NaOH solution.

The operando XAS experiment was carried out at the Swiss Light Source (SLS, Villigen, Switzerland), which operated at 2.4 GeV and 400 mA. The photoelectrochemical cell was aligned in such a way that the incident beam and the emitted fluorescence would enter and exit through the sample and silicon nitride window from the back side at an angle of ~45° (Figure 1). The incident beam provided by a 2.9T super bending magnet at the SuperXAS-X10DA beamline was collimated by a Si-coated mirror (at 2.8 mrad), which was also used for the reduction of higher harmonic contributions. The desired X-ray energies were scanned around the Fe K-edge (7110 eV) and Ni K-edge (8339 eV) using a Si (311) channel-cut monochromator to achieve good energy resolution at the pre-edge region. The beam was focused by an Rh-coated toroidal mirror at 2.8 mrad to a spot size of 1 mm × 0.2 mm ($H \times V$). The X-ray spectra were collected in fluorescence mode using an ion chamber filled with He/N_2 to measure the incoming beam intensity and an energy-dispersive five-element silicon drift detector mounted at 90° to the incoming beam to measure the fluorescence signal and the sample mounted at 45° (Figure S6).

XAS spectra were treated by subtracting a linear pre-edge background and were averaged and normalized to the edge jump of 1.0. EXAFS spectra using Origin software and were spline-fitted using IFEFFIT[35] through Athena graphical user interface. EXAFS scattering paths were calculated with FEFF6 using the Artemis graphical user interface[36] based on the crystallographic data of NiOOH and γ-FeOOH reported earlier.[37,38] The least-squares fitting of the Fourier-transformed EXAFS spectra was performed using a $\chi(k)$ range of 2−11 $Å^{-1}$ for the FT and using a k-weight of 3 via IFEFFIT[36] (more information in the Supporting Information Section 10).

RESULTS AND DISCUSSION

Oxygen Evolution Reaction on FTO/NiFeOOH and α-Fe_2O_3/NiFeOOH. Amorphous $Ni_{0.8}Fe_{0.2}OOH$ thin film-catalysts were prepared using the successive ionic adsorption and reaction (SILAR) method.[39,40] One of the advantages of using this "soft" deposition method is that it enables the deposition of an electrolyte-permeable electrocatalyst that forms adaptive junctions, which enable the photogenerated holes to be screened locally by the penetrating electrolyte ions, which in turn maximize the generated photovoltages.[17,29,30,41] Furthermore, previous work by our group has shown that FTO/NiFeOOH catalysts provide the lowest OER onset potential when the thickness of the catalytic overlayers ranged between 40 and 50 nm, and the concentration of iron in the catalyst is in the range of 20−30 atomic percentage.[40] These observations are also in agreement with several reports on the effect of Ni/Fe ratio on the OER performance of NiFeOOH electrocatalysts.[11,30,42,43] XPS analysis of Fe 2p and Ni 2p core levels in the as-prepared films confirms that Fe and Ni have 3+ and 2+ oxidation states, respectively (Figure S2). XRD analysis of the as-prepared FTO/NiFeOOH samples did not show diffraction peaks, which confirms the amorphous state of the electrocatalysts. Further XRD analysis after subjecting the films to 2 V_{RHE} polarization for 2 h did not show diffraction peaks either, which confirms that no long-range crystallinity was formed in the electrocatalysts upon potential application but does not rule out the possibility of small crystal formation with sizes in the nanometer scale that could not be detected with XRD (Figure S2). SEM images of the 50 nm films show the conformal and crack-free geometry of the films (Figure S2).

Linear sweep voltammetry (LSV) of FTO/$Ni_{0.8}Fe_{0.2}OOH$ showed a well-known Ni^{2+}/Ni^{3+} redox wave at ~1.4−1.5 V vs RHE, which was associated with the transition from $Ni(OH)_2$ to NiOOH.[11,42] Possible oxidation to higher valent $Ni^{3.5+/4+}$ species was also reported earlier.[14] The intensity of this charge-transfer wave increased with larger thin film thickness, which led to higher current densities and lower OER overpotentials as represented in Figure 1b. Deposition of 50 nm $Ni_{0.8}Fe_{0.2}OOH$ on 100 nm hematite thin films shifted the onset potential cathodically by 230 mV under one sun illumination (at 0.62 V vs RHE). More importantly, the current density did not decrease with respect to the bare hematite sample (Figure 1b). The photogenerated holes in the semiconductor under illumination contribute to the reduction in the applied potential and the subsequent photovoltage generation at the semiconductor/catalyst interface. This generated photovoltage can either be used to drive the OER at the semiconductor surface or alternatively, further drive the diffusion of holes from the semiconductor to the catalyst, which then drives the OER.[41] When illuminated from the glass side, i.e., back side, the performance was hampered due to the large α-Fe_2O_3 layer thickness and concomitant recombination in the hematite layer (Figure S5).

Operando XAS during FTO/$Ni_{0.8}Fe_{0.2}OOH$ Photoelectrochemical OER. One of the challenges of characterizing α-Fe_2O_3/$Ni_{0.8}Fe_{0.2}OOH$ is that both hematite and NiFeOOH contain iron species that could have similar or different oxidation states and local structures. Therefore, we first conducted operando XAS on the FTO/$Ni_{0.8}Fe_{0.2}OOH$ electrocatalyst and used the recorded Fe K-edge and Ni K-edge XANES of the as-prepared sample during (photo)-electrochemical OER and after the process as references for the linear combination fitting of the Fe K-edge of the α-Fe_2O_3/$Ni_{0.8}Fe_{0.2}OOH$. This allowed us to disentangle the XAS contribution from Fe in $Ni_{0.8}Fe_{0.2}OOH$ from that in α-Fe_2O_3 and also possibly from the interface. We also used this experiment to investigate the relaxation behavior of the Fe K-edge and Ni K-edge XANES in FTO/$Ni_{0.8}Fe_{0.2}OOH$.

https://doi.org/10.1021/acscatal.1c02566
ACS Catal. 2021, 11, 12324−12335

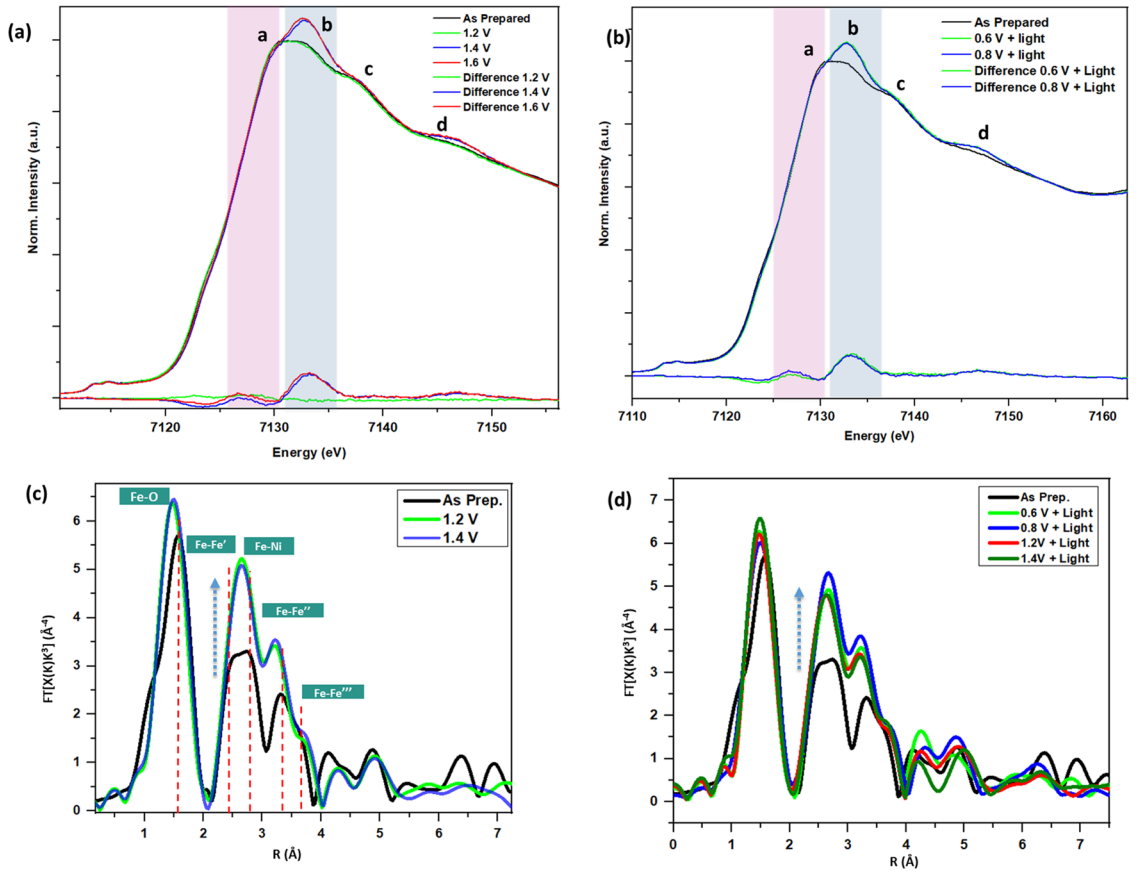

Figure 2. Operando XAS of iron in the α-Fe_2O_3/$Ni_{0.8}Fe_{0.2}OOH$ photoanode. (a) Iron K-edge XANES at different applied potentials in the dark (electrochemical, EC) and (b) under illumination (photoelectrochemical, PEC). (c) FT-EXAFS of Fe at different applied potentials in the dark and (d) under illumination.

The Fe K-edge and Ni K-edge XANES in Figures S7 and S8 contain multiple features: The pre-edge feature results from 1s → 3d quadrupole transitions, and its intensity increases by dipole contributions if the site is not centrosymmetric. The energy positions of both the pre-edge and the absorption edge provide information on the formal oxidation state of Ni in the electrocatalysts. Comparing the shape of the dipole-allowed 1s → 4p transitions in the near-edge region with known references and with electronic structure calculations can provide quantitative insight into the local geometric structure and ligand arrangement around the nickel atoms. Finally, the extended X-ray absorption fine structure (EXAFS) region yields quantitative information on the number and type of atoms around Ni as well as the bond distances between Ni and its surrounding atoms. In general, the results of the Fe K-edge and Ni K-edge XANES and EXAFS on FTO/$Ni_{0.8}Fe_{0.2}OOH$ during OER are in agreement with earlier reports on these electrocatalysts.[12,44] A detailed explanation of the observations and their interpretation can be found in Supporting Information Section 6. One final remarkable observation that we note on this system is regarding the recovery of the catalyst at open circuit potential, where we observed a reversal of the blue-shifted Ni K-edge spectra that represent the formation of γ-NiOOH phase to its original state that represents the α-$Ni(OH)_2$ phase. This process is slow and is fully completed within 1.5 h after reducing the applied potential (Figures S7 and S9). Closer examination of the Ni pre-edge and EXAFS after 0.5 and 1 h of opening the circuit shows that two different symmetries around Ni atoms co-exist during the relaxation process. This process is also observed in the Fe K-edge EXAFS but not in XANES (Figures S8 and S10). This observation provides an insight into the "self-healing" behavior of NiFeOOH after OER and points out to the dynamicity and reversibility of the Fe/Ni substation process, depending on the applied external potential. Recently, Kuai et al. conducted an extensive study to investigate the electronic origin of this catalyst's recovery mechanism and whether it could be accelerated.[45] They found that exposing NiFeOOH to an extended period of applied potential resulted in the segregation and dissolution of Fe ions to the electrolyte. Subsequent application of reduction potential resulted in the reincorporation of the Fe ions into the nickel hydroxide lattice within the catalyst.

Operando XAS during α-Fe_2O_3/$Ni_{0.8}Fe_{0.2}OOH$ Photoelectrochemical OER. As for the combined α-Fe_2O_3/$Ni_{0.8}Fe_{0.2}OOH$ photoanode, we showed in Figure 1 that the deposition of $Ni_{0.8}Fe_{0.2}OOH$ on hematite cathodically shifts the OER onset potential by ~300 mV. To understand the role of $Ni_{0.8}Fe_{0.2}OOH$ in reducing the OER onset potential in hematite, we conducted operando XAS measurements on the α-Fe_2O_3/$Ni_{0.8}Fe_{0.2}OOH$ photoanode under applied potential in both dark (electrochemical or EC) and under illumination (photoelectrochemical or PEC) conditions. At first glance, the iron K-edge XANES of the α-Fe_2O_3/$Ni_{0.8}Fe_{0.2}OOH$ sample looked visibly different from that of the FTO/$Ni_{0.8}Fe_{0.2}OOH$ sample (Figure 2a). Then, a clear spectral change in the Fe K-edge XANES could be observed starting from the application of a potential of 1.4 V (dark) and 0.6 V (illumination), where

https://doi.org/10.1021/acscatal.1c02566
ACS Catal. 2021, 11, 12324−12335

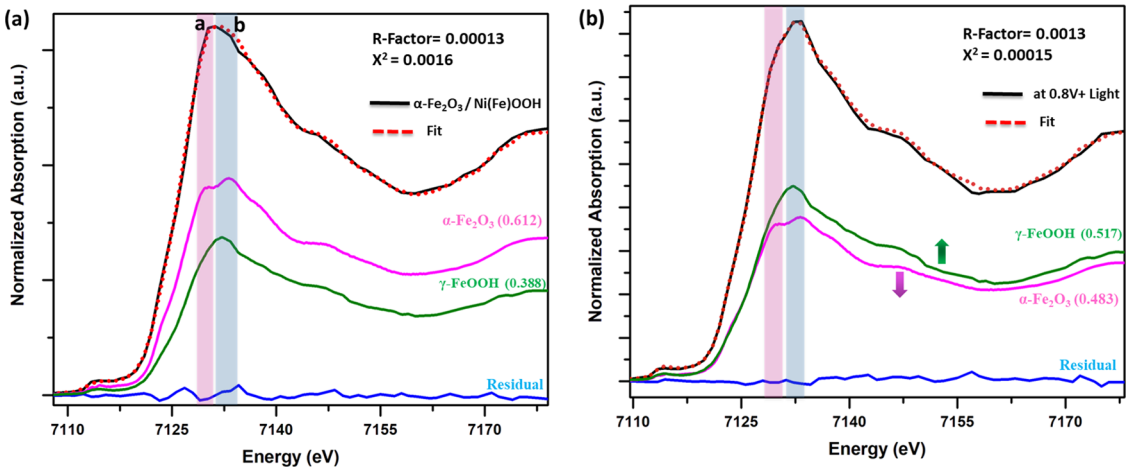

Figure 3. Linear combination fitting of Fe K-edge XANES in the α-Fe_2O_3/$Ni_{0.8}Fe_{0.2}OOH$ photoanode in the (a) as-prepared samples and in the (b) samples after applying 0.8 V under illumination. The fitting parameters, *R*-factor and χ^2 are shown for each fit and indicate that the fit is relatively accurate.

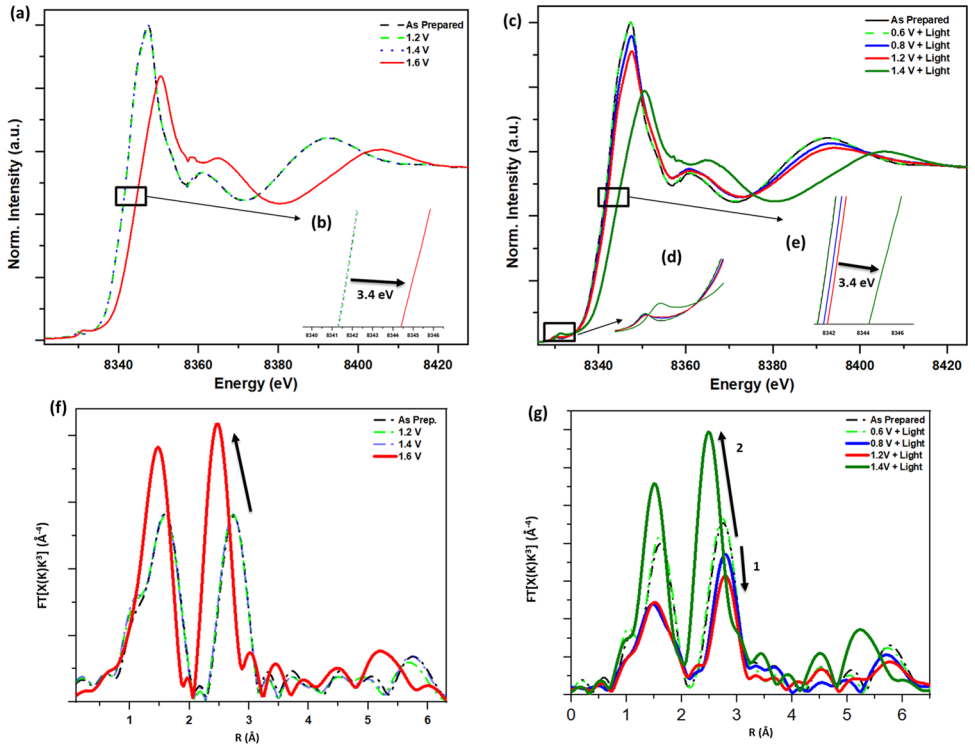

Figure 4. Operando Ni K-edge XAS of nickel in α-Fe_2O_3/$Ni_{0.8}Fe_{0.2}OOH$ photoanode. (a) Ni K-edge XANES at different applied potentials in the dark and (c) under illumination. (b, e) Inset to the K-edge showing the edge shift at 1.2 and 1.6 V applied potential. (d) Close up to the pre-edge region showing the 1s−3d transition during the OER applied potential. (f) FT-EXAFS of Ni at different applied potentials in the dark (EC) and (g) under illumination (PEC).

the spectral feature *b* increases in intensity, while features *a, c,* and *d* remain almost unchanged. This spectral change was also constant while applying higher potentials in the dark and under optical illumination conditions. To understand the origin of this spectral change, we conducted linear combination fitting (LCF) of multiple iron reference compounds and compared it with the Fe K-edge XANES spectra of the as-prepared sample and the sample at 0.6 V under illumination (Figure 3). A good fit was acquired for the as-prepared sample when we combined both the Fe K-edge XANES spectra of hematite (α-Fe_2O_3) and that of iron oxyhydroxide (γ-FeOOH also known as lepidocrocite) (Figure 3a). This is expected, given the fact that the emitted fluorescence signal contained information from iron species in both α-Fe_2O_3 and $Ni_{0.8}Fe_{0.2}OOH$ (where γ-FeOOH is known to be the dominant Fe phase for iron in the system, as we explained earlier in Supporting Information Section 6). Interestingly, an excellent fit of the Fe K-edge XANES spectrum at 0.8 V under illumination was acquired when the intensity of the α-Fe_2O_3 XANES was decreased and that of γ-FeOOH was increased by ∼13% (Figure 3b). These spectral changes of the Fe K-edge XANES and the subsequent LCF analysis directly indicate that upon external potential application, part of hematite was hydroxylated and structurally

https://doi.org/10.1021/acscatal.1c02566
ACS Catal. 2021, 11, 12324−12335

Table 1. Summary of the Spectral Change in the Ni and Fe XANES and EXAFS as a Function of Applied Potential in the Dark (EC) and Light (PEC) Conditions

α-Fe_2O_3/$Ni_{0.8}Fe_{0.2}$OOH photoanode as-prepared		oxidation state: Ni edge → Ni^{2+}/Fe edge → Fe^{3+} Fe XANES: 61% Fe_2O_3 and 39% FeOOH Ni EXAFS: Ni−O 2.08 Ni−M 3.12 → Ni^{2+} Fe EXAFS: Fe−O 2.01 Fe−M 3.04 → Fe^{3+}	
	applied voltage	**dark**	**light**
α-Fe_2O_3/$Ni_{0.8}Fe_{0.2}$OOH photoanode during OER	0.6 V_{RHE}		Fe XANES changes to 48% Fe_2O_3 and 52% FeOOH
	0.8 V_{RHE}		edge shift: Ni = 0.2 eV
	1.2 V_{RHE}		edge shift: Ni = 0.3 eV
	1.4 V_{RHE}	Fe XANES changes to 48% Fe_2O_3 and 52% FeOOH	edge shift: Ni = 3.4 eV → Ni^{3+} Ni−O 1.91 Ni−M 2.83 → Ni^{3+}
	1.6 V_{RHE}	edge shift: Ni = 3.4 eV → Ni^{3+} Ni−O 1.91 Ni−M 2.88 → Ni^{3+} Fe−O 1.92 Fe−M 2.89 → Fe^{3+}	

transformed into FeOOH at the Fe_2O_3/$Ni_{0.8}Fe_{0.2}$OOH interface.

The Fe K-edge FT-EXAFS of the as-prepared sample showed multiple Fe−M peaks (Figure 2c,d). By examining the FT-EXAFS fits of both FTO/α-Fe_2O_3 and FTO/$Ni_{0.8}Fe_{0.2}$OOH separately (Tables S1 and S2), we concluded that the Fe K-edge FT-EXAFS of the combined Fe_2O_3/$Ni_{0.8}Fe_{0.2}$OOH system is composed of the Fe−M peaks of both systems, where these peaks are representative of the Fe−Fe′ at 2.97 Å (α-Fe_2O_3), Fe−Ni/Fe at 3.04 Å ($Ni_{0.8}Fe_{0.2}$OOH), Fe−Fe″ at 3.41 Å (α-Fe_2O_3), Fe−Fe‴ at 3.71Å (α-Fe_2O_3), and Fe−O bond at 1.94 Å. The FT-EXAFS spectra were changed upon voltage application, where the M−M peaks were reduced to two main peaks: a Fe−M peak at 2.89 Å and another Fe−Fe peak at 3.4 Å, with similar Fe−O and Fe−M bond contraction observed to that in the case of FTO/$Ni_{0.8}Fe_{0.2}$OOH electrocatalysts. Correlating the observations from both Fe K-edge XANES and EXAFS shows that under solar-simulated optical illumination conditions, the Fe−O and Fe−M bond contractions and distortions took place directly after external potential application starting from 0.6 V_{RHE}, which is the same potential at which the structural transformation of ∼13% of hematite to FeOOH took place, as could be observed from XANES data. This is different from the EC "Dark" conditions, where this structural transformation took place at 0.2 V higher (at 1.4 V_{RHE}) than the potential needed to induce the Fe−O and Fe−M bond contractions and distortions as observed in EXAFS (at 1.2 V_{RHE}). This could mean that—in all cases—applying an external potential on α-Fe_2O_3/$Ni_{0.8}Fe_{0.2}$OOH results in distorting the Fe bonds with its neighboring atoms, but to induce the structural transformation of the surface of α-Fe_2O_3 to FeOOH, more holes generation is required, which is achieved either by applying higher external potential or via the optical illumination-induced photogenerated holes.

Examining the Ni K-edge XANES under applied potential in the "dark" condition showed a spectral response to the OER conditions similar to those observed earlier in the case of the FTO/$Ni_{0.8}Fe_{0.2}$OOH electrocatalyst. The XANES spectra of the as-prepared sample resembled that of Ni^{2+} species in α-$Ni(OH)_2$, which were then oxidized to $Ni^{3+/4+}$ (as in γ-NiOOH) at 1.6 V_{RHE} (Figure 4a). The spectral changes of Ni K-edge XANES under illumination were generally similar to that in the dark, with two important exceptions. First, the complete energy shift of the Ni K-edge under illumination has taken place at 1.4 V_{RHE}, which is 0.2 V lower than that in the dark conditions (Figure 4c). This is compatible with the LSV scans we showed earlier for α-Fe_2O_3/$Ni_{0.8}Fe_{0.2}$OOH, where the sharp increase in the generated photocurrent was observed at 1.4 V_{RHE} under illumination and at 1.6 V_{RHE} in the dark conditions (Figure 1b). This implies that the Ni oxidation process is directly related to the start of the OER.

Second, we also observe that unlike the sudden spectral shift that took place from 1.4 V_{RHE} to 1.6 V_{RHE} in the dark, the Ni K-edge started to change gradually under illumination while applying an external potential of 0.8 and 1.2 V, where the absorption edge started with a shift by 0.5 eV at 0.8 V_{RHE} accompanied by a slight distortion in the edge maximum until it shifted totally by 2.5 eV at 1.4 V_{RHE} (Figure 4). Furthermore, a similar spectral trend was observed in the Ni K-edge FT-EXAFS, where unlike the sharp increase in amplitude and the shortening of the bond lengths observed in the Ni−O and Ni−M bonds under the dark conditions, the amplitude of these two peaks decreased gradually first at 0.8 V_{RHE} and 1.2 V_{RHE} under illumination and then increased sharply at 1.4 V_{RHE} (Figure 4f,g). The sharp increase in the amplitude of both peaks at 1.6 V_{RHE} (dark) and at 1.4 V_{RHE} (illumination) and their smaller bond distances could be correlated with the oxidation of Ni during OER, and both spectral changes in XANES and EXAFS could be attributed to the injection of the (photo)generated holes from hematite to the NiFeOOH catalysts that resulted in the contraction of the Ni−O and Ni−M bonds and the distortion of the local environment around Ni during oxidation.

On the other hand, the observation of the small gradual shift in Ni XANES and the gradual reduction in the amplitudes of Ni−O and Ni−M bonds under illumination is related to and compatible with the broad anodic wave observed in the LSV of α-Fe_2O_3/$Ni_{0.8}Fe_{0.2}$OOH between 0.8 V_{RHE} and 1.4 V_{RHE}. Interpreting the origin of this phenomenon is not straightforward; since, on one hand, one might argue that this spectral change is the result of the direct photogenerated holes injection from hematite to NiFeOOH.[46] Then, these extracted holes are used up by NiFeOOH to carry out OER at 1.4 V_{RHE}, where Ni is oxidized. However, there are multiple issues with this assumption. First, the extent of the spectral change in Ni XANES and FT-EXAFS between 0.8 V_{RHE} and 1.4 V_{RHE} is relatively small and slow and does not seem to be compatible with the interaction of Ni species with the extracted holes that would work as excellent "catalysts" for triggering the oxidation of those Ni species. Second, NiFeOOH is an electrolyte-

https://doi.org/10.1021/acscatal.1c02566
ACS Catal. 2021, 11, 12324−12335

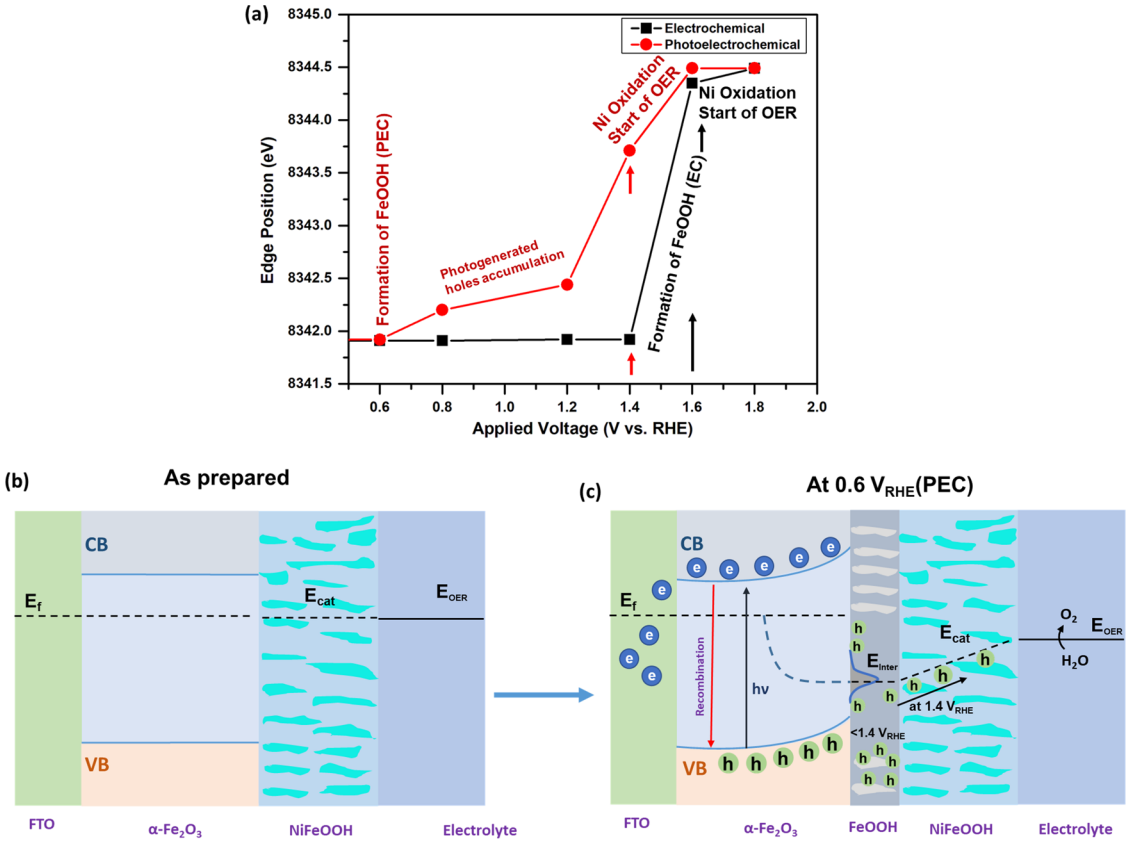

Figure 5. Mechanism of OER in α-Fe_2O_3/$Ni_{0.8}Fe_{0.2}OOH$. (a) Plot of the applied voltage (V vs RHE) vs the edge position of the Ni K-edge XAS in α-Fe_2O_3/$Ni_{0.8}Fe_{0.2}OOH$ photoanode at different applied potentials in the dark (EC) and under illumination (PEC). The plot shows the voltages at which FeOOH formation and Ni oxidation were observed from the Fe K-edge and Ni K-edge operando XAS data. (b) Schematic representation of the as-prepared photoanode (left) and the OER mechanism under illumination (right). E_f, E_{Inter}, E_{cat}, and E_{OER} represent the electrochemical potential (Fermi level) of the holes, the interface, the catalyst, and the electrolytic solution during OER, respectively.

permeable catalyst, where the redox ions are localized on the catalytic "islands" within the thin film and are in close proximity to, or interacting with, the semiconductor/catalyst interface.[17,30] Therefore, it is safe to think that once those photogenerated holes reach the interface, they would interact with the redox ions on the NiFeOOH catalytic islands, and OER would take place. These two processes should then take place simultaneously or within a few mV from each other, which is not the case here.

On the other hand, it is interesting to notice the clear remarkable difference between the spectral changes in Ni and Fe FT-EXAFS while increasing the applied potential under illumination (Table 1). While the Ni−O and Ni−M bonds exhibited a gradual decrease in amplitude and then a sharp increase in the amplitude accompanied by a bond length shortening at higher applied potential, the Fe−O and Fe−M bonds exhibited a monotonic sharp increase in amplitude under all applied potential conditions. We attribute this behavior to the effect of interfacial FeOOH formation on the holes transport from hematite to NiFeOOH. Since FeOOH is an insulator with poor electrical conductivity, it could possibly hold up or slow down the holes transport to the NiFeOOH, leading to the expansion of the NiO_6 octahedra and the reduction of the number of neighboring atoms around Ni while increasing the applied potential, which could be observed in EXAFS as a decrease in the amplitude of Ni−O and Ni−M bonds in the catalyst. It is also worth noting that the operando XAS observations do not confirm or deny the potential existence of Ni species in the interface, as the spectral changes that were observed in the Ni K-edge XAS are all related to the Ni oxidation and phase transformation taking place in Ni(Fe)OOH itself, as pointed out earlier in this study and in other studies as well.[8,12] We believe that if a cation diffusion phenomenon takes place, it will probably be compatible with the direction of the positive applied potential and the subsequent holes diffusion (i.e., from hematite to Ni(Fe)-OOH), as the Ni(Fe)OOH permeable catalyst sheets host a more chemically active environment compared to the compact hematite environment.

Role of Ni(Fe)OOH in Enhancing the OER over Hematite. The results of the operando XAS investigation discussed in the previous sections prove clearly that a FeOOH layer with an estimated thickness of ~13 ± 5 nm (estimated from LCF analysis) is formed at the interface α-Fe_2O_3/$Ni_{0.8}Fe_{0.2}OOH$. In this section, we will discuss three important implications based on the observations of this study: (1) the origin of formation of this layer, (2) its effect on the OER performance of hematite and NiFeOOH, and (3) the role of NiFeOOH in the OER process in light of the above observations.

Considering the results of this study altogether, we propose a possible OER mechanism in α-Fe_2O_3/$Ni_{0.8}Fe_{0.2}OOH$, whereupon optical illumination and at an applied potential of 0.6 V_{RHE}, a positive photovoltage gradient was created by lowering the holes' Fermi level that resulted in the photo-generated holes being transported from hematite to NiFeOOH, but most of the photogenerated holes do not

https://doi.org/10.1021/acscatal.1c02566
ACS Catal. 2021, 11, 12324−12335

reach the NiFeOOH catalyst at this potential (Figure 5a). Instead, part of these holes contributed to the formation of FeOOH phase at the α-Fe_2O_3/NiFeOOH interface (as observed from the structural distortion of the Fe K-edge maximum at 0.6 V_{RHE} under illumination and the change in the Fe−O and Fe−M amplitudes at the same potential), the other part of these holes (which we assume is the majority) were stored in the newly formed FeOOH layer. At 0.8 V_{RHE}, more photogenerated holes from hematite travel towards NiFeOOH, but the majority of those holes are instead further accumulated in FeOOH. This results in a gradual decrease in the amplitude of Ni−O and Ni−M bonds, which is an indication of the bond distortion and even a slight expansion in these bonds due to the presence of fewer neighbors around the Ni species while increasing the applied potential, as observed in the Ni K-edge EXAFS. This phenomenon is also accompanied by a gradual edge absorption shift to higher energy, as seen in XANES. These gradual effects increase further at 1.2 V_{RHE}, resulting in more holes being accumulated and stored in FeOOH, and only a small amount is released to NiFeOOH, leading to small photocurrent generation (as observed in the 0.8−1.4 region in the LSV scan in Figure 1c). However, at 1.4 V, the photogenerated holes accumulated in FeOOH are released to NiFeOOH. The release of the holes from FeOOH to NiFeOOH at this specific potential value is possibly due to the OER activation of more FeOOH species at higher applied potential in contrast to lower applied potential, as explained in detail by Boettcher and co-workers.[47] It is also possible that the Ni^{2+} oxidation to higher valence intermediates becomes more energetically favorable at this potential, thus allowing them to extract the holes stored within the FeOOH structure. Similar behavior was observed in CoO_xH_y catalysts by Li et al. and was explained further by Zhang et al.[48,49] We do not also exclude the simultaneous occurrence of both phenomena at this potential. Nevertheless, the release of these holes from FeOOH to NiFeOOH results in: (1) a contraction of the Ni−O and Ni−M bonds, (2) sharp increase in the amplitude of these bonds, and (3) a sudden blue shift of the Ni K-edge indicating the oxidation of Ni^{2+} to $Ni^{3+/4+}$ due to the interaction with the photogenerated holes. At this potential, OER takes place on NiFeOOH, and a sharp rise of the generated photocurrent is observed. As for the electrochemical (dark) conditions, we also observe the formation of FeOOH, albeit not directly upon potential application but at 1.4 V_{RHE} as observed in Fe K-edge XANES (the Fe bonds distortion takes place already at 1.2 V_{RHE}). The main difference between the EC and PEC conditions is the presence of a solar-simulated optical illumination source that excites the core electrons in hematite and generates a considerable quantity of holes. This photovoltage is probably responsible for inducing Ni and Fe bonding distortions at 0.2 V earlier in PEC compared to EC. These holes are also generated upon external potential application in the absence of optical illumination, but their concentration is much lower relative to the illumination conditions.[50] The positive voltage created by NiFeOOH during EC is also smaller, which leads to a slow transport rate of these holes to the catalyst until sufficient holes concentration reaches the NiFeOOH and drives the Ni redox process at the OER onset potential (at 1.4 V_{RHE}).

Based on the above observations and discussion, we suggest that the role of NiFeOOH to be mainly an OER catalyst which, due to its electrolyte permeability, provides an optimum voltage gradient for the photogenerated holes in hematite to travel to the electrolyte. The formed FeOOH layer acts then as a surface passivation overlayer that temporarily accumulates the photogenerated holes before releasing them to NiFeOOH (Figure 5b,c). It is important to mention here the important role the electrolyte-permeable and hydrated NiFeOOH catalyst may be playing in this structural transformation. We believe that the electrolyte permeability nature of NiFeOOH allows hydroxyl ions to build up within the catalyst and possibly reach the semiconductor/catalyst interface. More importantly, NiFeOOH facilitates hole extraction from hematite that is needed for the occurrence of this phase transformation process by reducing the potential required to drive the holes from hematite to the electrolyte.[17] We have conducted another operando XAS study on the bare hematite semiconductors during EC and PEC conditions, where we found that such phase transformation from α-Fe_2O_3 to FeOOH takes place only under optical illumination conditions and not in the dark. This observation underlines the importance of NiFeOOH catalysts in the efficient holes extraction process from hematite that leads to FeOOH formation even under EC (dark) conditions. The results of the operando XAS on bare hematite semiconductor will be discussed in detail elsewhere.

In addition, the above results also highlight the role of FeOOH not only as a surface passivation layer but also as a "hole regulator" within the α-Fe_2O_3/NiFeOOH system. Hajibabaei et al. investigated the OER performance of $Ni_{75}Fe_{25}OOH$ and $Ni_{25}Fe_{75}OOH$ catalysts deposited on very thin (~30 nm) α-Fe_2O_3 samples made by atomic layer deposition (ALD) and electrodeposition (ED).[51] Both catalysts showed comparable performance in the case of ALD-hematite. As for the ED-hematite, the $Ni_{25}Fe_{75}OOH$ showed lower OER overpotential than $Ni_{75}Fe_{25}OOH$. This is remarkable, given the several reports in the literature on the superior OER performance of $Ni_{25}Fe_{75}OOH$.[11,16,27] They attributed the lower performance of $Ni_{75}Fe_{25}OOH$ to the formation of the hematite-NiO_x layer at the interface that acts as a recombination center, while $Ni_{25}Fe_{75}OOH$ effectively collected the photogenerated holes by passivating the hematite surface states. It is important to note here that the $Ni_{25}Fe_{75}OOH$ consists of two separate phases; a FeOOH phase and a Fe-doped NiOOH phase.[12,51] In another study, Kim et al. reported a remarkable improvement in the OER performance in $BiVO_4$ when a FeOOH layer was deposited between the BiVO4 semiconductor and the NiOOH catalyst. They attributed this performance improvement to the role that FeOOH played in reducing interfacial recombination, hence increasing the holes concentration available for OER.[52] This observation could explain the results of Hajibabaei et al. in which the superior performance of $Ni_{25}Fe_{75}OOH$ could be due to the surface state passivation by FeOOH, which enabled an optimum holes extraction by the other phase, namely NiFeOOH. In light of our observations, we also believe that the observed superior OER performance in the Fe-rich catalyst is due to the FeOOH−NiFeOOH phase segregation in this catalyst, while they did not observe similar performance in the Ni-rich catalyst because the thin film of the hematite semiconductor they used was probably too small (~30 nm) to form the optimum FeOOH interfacial layer. Finally, both catalysts provided comparable OER performance on the ALD-hematite sample, possibly due to the packed surface nature of the ALD-prepared films that did not allow the electrolytic ions

https://doi.org/10.1021/acscatal.1c02566
ACS Catal. 2021, 11, 12324−12335

to pass through the semiconductor and facilitate FeOOH formation.

One might ask whether adding FeOOH always improves the OER performance on photoanodes. We believe that the answer to this question depends on the thickness of the FeOOH in the system, which in turn depends on the thickness of the underlying hematite semiconductor and the Fe-concentration in the NiFeOOh overlayer. FeOOH itself has a higher OER turnover frequency (TOF) than CoOOH and NiOH catalysts that increases further at higher applied potential.[53] However, its low electrical conductivity hinders its OER performance and makes it act as an insulator. Furthermore, increasing its thickness affects its TOF even at higher applied potential, as was shown by Burke et al.[54] This thickness increase could possibly impede the holes transport, resulting in the need for higher potential application to release these holes to the NiFeOOH catalyst for OER to take place. If this speculation is true, it could explain why having a high Fe concentration in NiFeOOH shifts the OER onset potential to higher values rather than to lower values, since it is known that NiFeOOH with high Fe concentration (>50% Fe concentration) tends to form mixed FeOOH/NiFeOOH phases, where the OER inactive γ-FeOOH is the dominant phase (with the exception of Hajibabaei et al. study).[11,12] Therefore, we speculate, based on the results of this study, that having a thin interfacial layer of FeOOH could be beneficial to the overall OER activity of the α-Fe_2O_3/$Ni_{0.8}Fe_{0.2}$OOH because of its role in the hematite surface passivation, possible charging prevention, and more holes extraction. However, increasing the thickness of this layer beyond a certain limit may hinder the holes transport to NiFeOOH due to the poor electrical conductivity of FeOOH and may lead to charge trapping and recombination effects, which results in shifting the OER overpotential to higher values. An interesting future study to further investigate this phenomenon is to conduct a combined operando XAS and LSV investigation on α-Fe_2O_3/FeOOH/$Ni_{0.8}Fe_{0.2}$OOH samples, where only the thickness of the FeOOH interlayer is changed. If our above assumption is true, then the results of this experiment will show that the thicker the FeOOH is, the more the OER onset potential to higher values, and possibly, the Ni oxidation potential will also shift as well.

CONCLUSIONS

In this study, we conducted operando XAS analysis on the combined α-Fe_2O_3/$Ni_{0.8}Fe_{0.2}$OOH photoanode during (photo)electrochemical OER, where we observed a spontaneous formation of an interfacial FeOOH layer that forms upon potential application. Since the formation of this layer is accelerated further under optical illumination conditions, we believe that the formation of this layer is directly related to the ability of NiFeOOH to extract the (photo)generated holes from hematite as well as facilitating the interfacial interaction with the electrolytic ions via its porous structure. This interfacial FeOOH layer could be playing a role in the surface passivation and efficient holes extraction from hematite, which leads to high photocurrent generation during OER, as observed in previous studies. However, it also plays a detrimental role by holding up and slowing down the transport of these holes to NiFeOOH because of its intrinsically poor electrical conductivity, resulting in delaying the start of OER on NiFeOOH. This detrimental effect becomes more severe when the thickness of these layers is increased. We believe that identifying the origin of the formation of this interfacial FeOOH layer and its role in dictating the OER dynamics on NiFeOOH will help in further understanding the role that NiFeOOH plays during OER and will also explain some of the apparently contradicting results surrounding the effect of Fe concentration on the OER performance of NiFeOOH as well as the performance improvement of other investigated systems that include FeOOH.

ASSOCIATED CONTENT

Supporting Information

The Supporting Information is available free of charge at https://pubs.acs.org/doi/10.1021/acscatal.1c02566.

Catalyst and semiconductor preparation, physical characterization of the samples, operando reactor and electrodes designs, detailed OER electrochemical characterization, operando XAS results on FTO/$Ni_{0.8}Fe_{0.2}$OOH, full set of operando XANES spectra, XAS of references, and FT-EXAFS fitting parameters (PDF)

AUTHOR INFORMATION

Corresponding Authors

Ahmed S. M. Ismail − *Inorganic Chemistry and Catalysis Group, Utrecht University, 3584 CG Utrecht, The Netherlands;* orcid.org/0000-0002-2282-1665; Email: ahmedwork@live.com

Frank M. F. de Groot − *Inorganic Chemistry and Catalysis Group, Utrecht University, 3584 CG Utrecht, The Netherlands;* orcid.org/0000-0002-1340-2186; Email: f.m.f.degroot@uu.nl

Authors

Ivan Garcia-Torregrosa − *Inorganic Chemistry and Catalysis Group, Utrecht University, 3584 CG Utrecht, The Netherlands; TNO Energy Transition, 1755 LE Petten, The Netherlands*

Jeroen C. Vollenbroek − *BIOS Lab on a Chip Group, MESA + Institute of Nanotechnology, University of Twente, 7522 NB Enschede, The Netherlands*

Laura Folkertsma − *TNO Energy Transition, 1755 LE Petten, The Netherlands*

Johan G. Bomer − *BIOS Lab on a Chip Group, MESA+ Institute of Nanotechnology, University of Twente, 7522 NB Enschede, The Netherlands*

Ties Haarman − *Inorganic Chemistry and Catalysis Group, Utrecht University, 3584 CG Utrecht, The Netherlands*

Mahnaz Ghiasi − *Inorganic Chemistry and Catalysis Group, Utrecht University, 3584 CG Utrecht, The Netherlands*

Meike Schellhorn − *Optics/Short Wavelengths Department, Laser-Laboratorium Göttingen e.V., 37077 Göttingen, Germany*

Maarten Nachtegaal − *Paul Scherrer Institute, 5232 Villigen, Switzerland;* orcid.org/0000-0003-1895-9626

Mathieu Odijk − *BIOS Lab on a Chip Group, MESA+ Institute of Nanotechnology, University of Twente, 7522 NB Enschede, The Netherlands*

Albert van den Berg − *BIOS Lab on a Chip Group, MESA+ Institute of Nanotechnology, University of Twente, 7522 NB Enschede, The Netherlands*

Bert M. Weckhuysen − *Inorganic Chemistry and Catalysis Group, Utrecht University, 3584 CG Utrecht, The Netherlands;* orcid.org/0000-0001-5245-1426

Complete contact information is available at:
https://pubs.acs.org/10.1021/acscatal.1c02566

Notes

The authors declare no competing financial interest.

■ ACKNOWLEDGMENTS

This work was supported by the Netherlands Center for Multiscale Catalytic Energy Conversion (MCEC), an NWO Gravitation programme funded by the Ministry of Education, Culture, and Science of the Government of the Netherlands. This project has also received partial funding from the EU-H2020 Research and Innovation Programme under Grant Agreement No. 654360, having benefitted from the access provided by the Paul Scherrer Institute, Villigen, Switzerland, to the SuperXAS beamline at the SLS within the framework of the NFFA-Europe Transnational Access Activity.

■ REFERENCES

(1) Walter, M. G.; Warren, E. L.; Mckone, J. R.; Boettcher, S. W.; Mi, Q. X.; Santori, E. A.; Lewis, N. S. Solar Water Splitting Cells. *Chem. Rev.* **2010**, *110*, 6446−6473.
(2) Lee, Y.; Suntivich, J.; May, K. J.; Perry, E. E.; Shao-Horn, Y. Synthesis and Activities of Rutile IrO_2 and RuO_2 Nanoparticles for Oxygen Evolution in Acid and Alkaline Solutions. *J. Phys. Chem. Lett.* **2012**, *3*, 399−404.
(3) McCrory, C. C. L.; Jung, S.; Peters, J. C.; Jaramillo, T. F. Benchmarking Heterogeneous Electrocatalysts for the Oxygen Evolution Reaction. *J. Am. Chem. Soc.* **2013**, *135*, 16977−16987.
(4) Gong, M.; Dai, H. A Mini Review of NiFe-Based Materials as Highly Active Oxygen Evolution Reaction Electrocatalysts. *Nano Res.* **2015**, *8*, 23−39.
(5) Corrigan, D. A. The Catalysis of the Oxygen Evolution Reaction by Iron Impurities in Thin Film Nickel Oxide Electrodes. *J. Electrochem. Soc.* **1987**, *134*, 377−384.
(6) Lu, X.; Zhao, C. Electrodeposition of Hierarchically Structured Three-Dimensional Nickel−Iron Electrodes for Efficient Oxygen Evolution at High Current Densities. *Nat. Commun.* **2015**, *6*, No. 6616.
(7) Long, X.; Li, J.; Xiao, S.; Yan, K.; Wang, Z.; Chen, H.; Yang, S. A Strongly Coupled Graphene and FeNi Double Hydroxide Hybrid as an Excellent Electrocatalyst for the Oxygen Evolution Reaction. *Angew. Chem., Int. Ed.* **2014**, *53*, 7584−7588.
(8) Feng, C.; Faheem, M. B.; Fu, J.; Yequan, X.; Changli, L.; Yanbo, L. Fe-Based Electrocatalysts for Oxygen Evolution Reaction: Progress and Perspectives. *ACS Catal.* **2020**, *10*, 4019−4047.
(9) Merrill, M. D.; Dougherty, R. C. Metal Oxide Catalysts for the Evolution of O_2 from H_2O. *J. Phys. Chem. C* **2008**, *112*, 3655−3666.
(10) Morales-Guio, C. G.; Mayer, M. T.; Yella, A.; Tilley, S. D.; Graetzel, M.; Hu, X. An Optically Transparent Iron Nickel Oxide Catalyst for Solar Water Splitting. *J. Am. Chem. Soc.* **2015**, *137*, 9927−9936.
(11) Trotochaud, L.; Young, S. L.; Ranney, J. K.; Boettcher, S. W. Nickel−Iron Oxyhydroxide Oxygen-Evolution Electrocatalysts: The Role of Intentional and Incidental Iron Incorporation. *J. Am. Chem. Soc.* **2014**, *136*, 6744−6753.
(12) Friebel, D.; Louie, M. W.; Bajdich, M.; Sanwald, K. E.; Cai, Y.; Wise, A. M.; Cheng, M.; Sokaras, D.; Weng, T.; Alonso-Mori, R.; Davis, R. C.; Bargar, J. R.; Nørskov, J. K.; Nilsson, A.; Bell, A. T. Identification of Highly Active Fe Sites in (Ni,Fe)OOH for Electrocatalytic Water Splitting. *J. Am. Chem. Soc.* **2015**, *137*, 1305−1313.
(13) Ahn, H. S.; Bard, A. J. Surface Interrogation Scanning Electrochemical Microscopy of $Ni_{1-x}Fe_xOOH$ ($0 < x < 0.27$) Oxygen Evolving Catalyst: Kinetics of the "fast" Iron Sites. *J. Am. Chem. Soc.* **2016**, *138*, 313−318.
(14) Li, N.; Bediako, D. K.; Hadt, R. G.; Hayes, D.; Kempa, T. J.; von Cube, F.; Bell, D. C.; Chen, L. X.; Nocera, D. G. Influence of Iron Doping on Tetravalent Nickel Content in Catalytic Oxygen Evolving Films. *Proc. Natl. Acad. Sci. U.S.A.* **2017**, *114*, 1486−1491.
(15) Suen, N.-T.; Hung, S.-F.; Quan, Q.; Zhang, N.; Xu, Y.-J.; Chen, H. M. Electrocatalysis for The Oxygen Evolution Reaction: Recent Development and Future Perspectives. *Chem. Soc. Rev.* **2017**, *46*, 337−365.
(16) Wu, L.; Yu, L.; Xiao, X.; Zhang, F.; Song, S.; Chen, S.; Ren, Z. Recent Advances in Self-Supported Layered Double Hydroxides for Oxygen Evolution Reaction. *Research* **2020**, *2020*, No. 3976278.
(17) Nellist, M. R.; Laskowski, F. A. L.; Lin, F.; Mills, T. J.; Boettcher, S. W. Semiconductor−Electrocatalyst Interfaces: Theory, Experiment, and Applications in Photoelectrochemical Water Splitting. *Acc. Chem. Res.* **2016**, *49*, 733−740.
(18) Chen, D.; Liu, Z.; Zhang, S. Enhanced PEC Performance of Hematite Photoanode Coupled with Bimetallic Oxyhydroxide NiFeOOH Through a Simple Electroless Method. *Appl. Catal., B* **2020**, *265*, No. 118580.
(19) Carroll, G. M.; Gamelin, D. R. Kinetic Analysis of Photoelectrochemical Water Oxidation by Mesostructured Co-Pi/α-Fe_2O_3 Photoanodes. *J. Mater. Chem. A* **2016**, *4*, 2986−2994.
(20) Carroll, G. M.; Zhong, D. K.; Gamelin, D. R. Mechanistic Insights into Solar Water Oxidation by Cobalt-Phosphate-Modified α-Fe_2O_3 Photoanodes. *Energy Environ. Sci.* **2015**, *8*, 577−584.
(21) Klahr, B.; Gimenez, S.; Fabregat-Santiago, F.; Bisquert, J.; Hamann, T. Photoelectrochemical and Impedance Spectroscopic Investigation of Water Oxidation with "Co−Pi"-Coated Hematite Electrodes. *J. Am. Chem. Soc.* **2012**, *134*, 16693−16700.
(22) Zachäus, C.; Abdi, F. F.; Peter, L. M.; Van De Krol, R. Photocurrent of $BiVO_4$ is Limited by Surface Recombination, not Surface Catalysis. *Chem. Sci.* **2017**, *8*, 3712−3719.
(23) Liu, R.; Zheng, Z.; Spurgeon, J.; Yang, X. G. Enhanced Photoelectrochemical Water-Splitting Performance of Semiconductors by Surface Passivation Layers. *Energy Environ. Sci.* **2014**, *7*, 2504−2517.
(24) Li, W.; He, D.; Sheehan, S. W.; He, Y. M.; Thorne, J. E.; Yao, X. H.; Brudvig, G. W.; Wang, D. W. Comparison of Heterogenized Molecular and Heterogeneous Oxide Catalysts for Photoelectrochemical Water Oxidation. *Energy Environ. Sci.* **2016**, *9*, 1794−1802.
(25) de Respinis, M.; Joya, K. S.; De Groot, H. J. M.; D'Souza, F.; Smith, W. A.; van de Krol, R.; Dam, B. Solar Water Splitting Combining a $BiVO_4$ Light Absorber with a Ru-Based Molecular Cocatalyst. *J. Phys. Chem. C* **2015**, *119*, 7275−7281.
(26) Thorne, J. E.; Jang, J.-W.; Liu, E. Y.; Wang, D. Understanding the Origin of Photoelectrode Performance Enhancement by Probing Surface Kinetics. *Chem. Sci.* **2016**, *7*, 3347−3354.
(27) Lee, J.; Seo, D.; Won, S.; Chung, T. D. Understanding the Role of Nickel−Iron (Oxy)hydroxide (NiFeOOH) Electrocatalysts on Hematite Photoanodes. *Sustainable Energy Fuels* **2021**, *5*, 501−508.
(28) Malara, F.; Minguzzi, A.; Marelli, M.; Morandi, S.; Psaro, R.; Dal Santo, V.; Naldoni, A. α-Fe_2O_3/NiOOH: An Effective Heterostructure for Photoelectrochemical Water Oxidation. *ACS Catal.* **2015**, *5*, 5292−5300.
(29) Laskowski, F. A. L.; Nellist, M. R.; Qiu, J.; Boettcher, S. W. Metal Oxide/(oxy)hydroxide Overlayers as Hole Collectors and Oxygen-Evolution Catalysts on Water-Splitting Photoanodes. *J. Am. Chem. Soc.* **2019**, *141*, 1394−1405.
(30) Qiu, J. J.; Hajibabaei, H.; Nellist, M. R.; Laskowski, F. A. L.; Oener, S. Z.; Hamann, T. W.; Boettcher, S. W. Catalyst Deposition on Photoanodes: The Roles of Intrinsic Catalytic Activity, Catalyst Electrical Conductivity, and Semiconductor Morphology. *ACS Energy Lett.* **2018**, *3*, 961−969.
(31) George, K.; Zhang, X.; Bieberle-Hütter, A. Why does NiOOH Cocatalyst Increase the Oxygen Evolution Activity of α-Fe_2O_3? *J. Chem. Phys.* **2019**, *150*, No. 041729.
(32) van Oversteeg, C. H. M.; Doan, H. Q.; de Groot, F. M. F.; Cuk, T. In Situ X-ray Absorption Spectroscopy of Transition Metal Based Water Oxidation Catalysts. *Chem. Soc. Rev.* **2017**, *46*, 102−125.

(33) Braun, A.; Hu, Y.; Boudoire, F.; Bora, D. K.; Sarma, D. D.; Grätzel, M.; Eggleston, C. M. The Electronic, Chemical and Electrocatalytic Processes and Intermediates on Iron Oxide Surfaces during Photoelectrochemical Water Splitting. *Catal. Today* **2016**, *260*, 72−81.
(34) Braun, A.; Hu, Y.; Boudoire, F.; Bora, D. K.; Sarma, D. D.; Grätzel, M.; Eggleston, C. M.; et al. Direct Observation of Two Electron Holes in a Hematite Photoanode during Photoelectrochemical Water Splitting. *J. Phys. Chem. C* **2012**, *116*, 16870−16875.
(35) Newville, M. IFEFFIT: Interactive XAFS Analysis and FEFF Fitting. *J. Synchrotron Radiat.* **2001**, *8*, 322−324.
(36) Ravel, B.; Newville, M. ATHENA, ARTEMIS, HEPHAESTUS: Data Analysis for X-ray Absorption Spectroscopy using IFEFFIT. *J. Synchrotron Radiat.* **2005**, *12*, 537−541.
(37) Christensen, H.; Christensen, A. Hydrogen bonds of gamma-FeOOH. *Acta Chem. Scand.* **1978**, *32A*, 87−88.
(38) Ramesh, T. N.; Kamath, P. V.; Shivakumara, C. Classification of Stacking Faults and Their Stepwise Elimination during the Disorder –> Order Transformation of Nickel Hydroxide. *Acta Crystallogr., Sect. B: Struct. Sci., Cryst. Eng. Mater.* **2006**, *62*, 530−536.
(39) Bediako, D. K.; Lassalle-Kaiser, B.; Surendranath, Y.; Yano, J.; Yachandra, V. K.; Nocera, D. G. Structure−Activity Correlations in a Nickel−Borate Oxygen Evolution Catalyst. *J. Am. Chem. Soc.* **2012**, *134*, 6801−6809.
(40) Garcia-Torregrosa, I.; Goryachev, A.; Hofmann, J. P.; Hensen, E. J. M.; Weckhuysen, B. M. Efficient and Highly Transparent Ultra-Thin Nickel-Iron Oxy-hydroxide Catalyst for Oxygen Evolution Prepared by Successive Ionic Layer Adsorption and Reaction. *ChemPhotoChem* **2019**, *3*, 1050−1054.
(41) Qiu, J.; Hajibabaei, H.; Nellist, M. R.; Laskowski, F. A.; Hamann, T. W.; Boettcher, S. W. Direct in Situ Measurement of Charge Transfer Processes During Photoelectrochemical Water Oxidation on Catalyzed Hematite. *ACS Cent. Sci.* **2017**, *3*, 1015−1025.
(42) Louie, M. W.; Bell, A. T. An Investigation of Thin-Film Ni−Fe Oxide Catalysts for the Electrochemical Evolution of Oxygen. *J. Am. Chem. Soc.* **2013**, *135*, 12329−12337.
(43) Qiu, Y.; Xin, L.; Li, W. Electrocatalytic Oxygen Evolution over Supported Small Amorphous Ni−Fe Nanoparticles in Alkaline Electrolyte. *Langmuir* **2014**, *30*, 7893−7901.
(44) Balasubramanian, M.; Melendres, C. A.; Mini, S. X-ray Absorption Spectroscopy Studies of the Local Atomic and Electronic Structure of Iron Incorporated into Electrodeposited Hydrous Nickel Oxide Films. *J. Phys. Chem. B* **2000**, *104*, 4300−4306.
(45) Kuai, C.; Xu, Z.; Xi, C.; Hu, A.; Yang, Z.; Zhang, Y.; Sun, C.-J.; Li, L.; Sokaras, D.; Dong, C.; Qiao, S.-Z.; Du, X.-X.; Feng, L. Phase Segregation Reversibility in Mixed-Metal Hydroxide Water Oxidation Catalysts. *Nat. Catal.* **2020**, *3*, 743−753.
(46) Tsyganok, A.; Ghigna, P.; Minguzzi, A.; Naldoni, A.; Murzin, V.; Caliebe, W.; Rothschild, A.; Ellis, D. S. Operando X-ray Absorption Spectroscopy (XAS) Observation of Photoinduced Oxidation in FeNi (Oxy)hydroxide Overlayers on Hematite (α-Fe_2O_3) Photoanodes for Solar Water Splitting. *Langmuir* **2020**, *36*, 11564−11572.
(47) Zou, S.; Burke, M. S.; Kast, M. G.; Fan, J.; Danilovic, N.; Boettcher, S. W. Fe (Oxy)hydroxide Oxygen Evolution Reaction Electrocatalysis: Intrinsic Activity and the Roles of Electrical Conductivity, Substrate, and Dissolution. *Chem. Mater.* **2015**, *27*, 8011−8020.
(48) Li, J.; Wan, W.; Triana, C. A.; Novotny, Z.; Osterwalder, J.; Erni, R.; Patzke, G. R. Dynamic Role of Cluster Cocatalysts on Molecular Photoanodes for Water Oxidation. *J. Am. Chem. Soc.* **2019**, *141*, 12839−12848.
(49) Zhang, J.; Cui, J.; Eslava, S. Oxygen Evolution Catalysts at Transition Metal Oxide Photoanodes: Their Differing Roles for Solar Water Splitting. *Adv. Energy Mater.* **2021**, *11*, No. 2003111.
(50) Iandolo, B.; Wickman, B.; Zorić, I.; Hellman, A. The Rise of Hematite: Origin and Strategies to Reduce the High Onset Potential for the Oxygen Evolution Reaction. *J. Mater. Chem. A* **2015**, *3*, 16896−16912.
(51) Hajibabaei, H.; Schon, A. R.; Hamann, T. W. Interface Control of Photoelectrochemical Water Oxidation Performance with $Ni_{1-x}Fe_xO_y$ Modified Hematite Photoanodes. *Chem. Mater.* **2017**, *29*, 6674−6683.
(52) Kim, T. W.; Choi, K. Nanoporous $BiVO_4$ Photoanodes with Dual-Layer Oxygen Evolution Catalysts for Solar Water Splitting. *Science* **2014**, *343*, 990−994.
(53) Burke, M. S.; Zou, S.; Enman, L. J.; Kellon, J. E.; Gabor, C. A.; Pledger, E.; Boettcher, C. W. Revised Oxygen Evolution Reaction Activity Trends for First-Row Transition-Metal (Oxy)hydroxides in Alkaline Media. *J. Phys. Chem. Lett.* **2015**, *6*, 3737−3742.
(54) Burke, M. S.; Kast, M. G.; Trotochaud, L.; Smith, A. M.; Boettcher, S. W. Cobalt-Iron (Oxy)hydroxide Oxygen Evolution Electrocatalysts: The Role of Structure and Composition on Activity, Stability, and Mechanism. *J. Am. Chem. Soc.* **2015**, *137*, 3638−3648.

https://doi.org/10.1021/acscatal.1c02566
ACS Catal. 2021, 11, 12324−12335